ACS OMEGA

http://pubs.acs.org/journal/acsodf

Article

Numerical Simulation of the Microscopic Plugging Mechanism and Particle Flow Process of the Microsphere System

Renyi Lin* and Lei Sun

Cite This: *ACS Omega* 2022, 7, 46983−46991

Read Online

ACCESS | Metrics & More | Article Recommendations

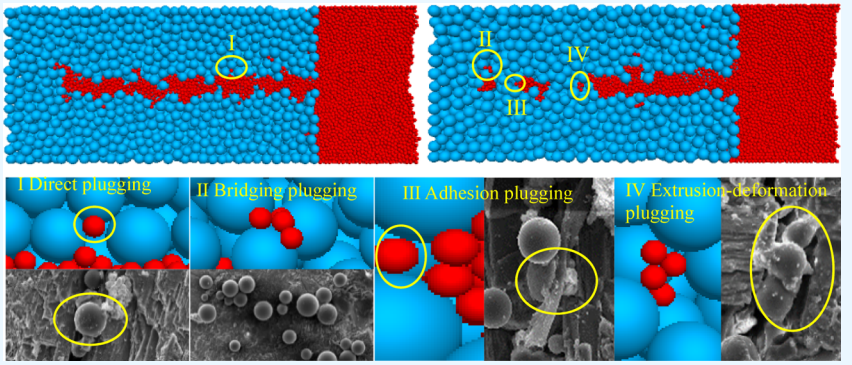

ABSTRACT: The microsphere system has small initial particle size, excellent swelling performance, simple manufacturing process, and strong plugging ability. It has great application potential in the field of plugging and profile control of deep reservoirs. Microspheres can effectively plug the pores of fractured cores, inhibit the rapid breakthrough process, and improve the sweep efficiency of the injected fluids. However, the microscopic plugging mechanism of microspheres on fractured cores is still unclear. In this study, the distribution of microspheres after plugging was observed through specially prepared core models. Furthermore, the microscopic plugging mechanism of microspheres in fractured reservoir cores was clarified, including direct microsphere plugging, cluster bridging plugging, adhesion plugging, extrusion-deformation plugging, and extrusion-crushing plugging. Then, particle flow simulation software was used to establish the fluid−solid coupling model of microsphere plugging, and then, the numerical simulation of the plugging process was realized by Python module programming. Through this study, the plugging effect of microspheres under different fracture opening conditions was clarified. Moreover, the effects of injection pressure difference, fracture width, and particle size ratio on the fluid−solid structures of microsphere plugging were analyzed. The results show that the smaller the particle size ratio, the greater the injection pressure difference, the fracture width, and the reduction magnitudes in fracture porosity and core permeability and the higher the plugging rate. The numerical simulation results well support the microsphere plugging mechanism obtained by experiments. The results of this study can provide theoretical and technical support for the development of deep profile control and flooding and enhanced oil recovery technology of the polymer microsphere dispersion system in fractured low-permeability reservoirs.

1. INTRODUCTION

Water (or gas) flooding is an important means to ensure stable production of oil and gas. However, serious water invasion often occurs in fractured reservoirs, which seriously affects the recovery of oil and gas resources.[1,2] Studies have shown that polymer microspheres can achieve effective plugging of reservoirs. According to the particle size, the microspheres can realize direct, deformable, shear separation, bridging, and adhesive plugging in the reservoir.[3] They can enter the deep reservoir via the fracture network and realize multidimensional step-by-step plugging and profile control.[4] Lei et al. (2007)[5,6] found that the microspheres rely on the resistance of physical barriers in the pores to control the water flow and the swept volume. Moreover, the microspheres can pass through the throats under the action of elastic deformation and create resistance to the water flow at the adjacent throats. Furthermore, the microspheres can continuously migrate to the deep part of the oil layers. Liu (2010)[7] found that in the deep profile control and oil flooding process, nano/micron-scale polymer microspheres can expand, bond, and coalesce

Received: September 21, 2022
Accepted: November 21, 2022
Published: December 5, 2022

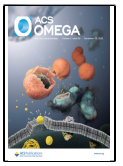

ACS Publications

© 2022 The Authors. Published by American Chemical Society

https://doi.org/10.1021/acsomega.2c06088
ACS Omega 2022, 7, 46983−46991

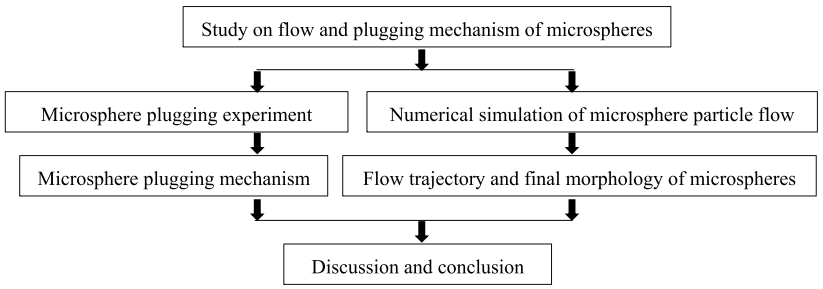

Figure 1. General sketch of the problem under study.

with each other and preferentially plug the high-permeability layers. The swelling characteristics of the microspheres can make the flow diversion ability of the microspheres increase after entering the deep oil layers. Fan (2012)[8] found that the streamlines formed by the plugging of polymer microspheres would turn, and the low-permeability layers that had not been affected before were affected. Then, the sweep efficiency of the injected water and the production capacity of the oil wells are significantly improved.[9,10]

Simulation of the particle flow process is often used in the fluid−solid coupling in soil. In addition, some researchers have also used it to simulate the fluid−solid coupling in the process of sand production. However, there are few reports and references on the application of particle flow simulation in leakage and channeling prevention of microspheres. Common fluid-structure interaction algorithms include Computational Fluid Dynamics (CFD)-Discrete Element Method (DEM),[11−16] Lattice Boltzmann Method (LBM)-DEM,[17−20] and Dynamic Fluid Mesh (DFM)-DEM methods. Besides CFD and LBM, there are other methods such as REV,[21] SPH,[22] pore network method[23,24] that can also be used to solve the fluid-structure interaction problem in DEM. However, none of these methods can well simulate the fluid−solid coupling mechanism during the plugging and anti-channeling process. Therefore, in this paper, the DFM-DEM method is used to study the fluid−solid coupling problem of microspheres.[25,26] This method has high computational efficiency and can well solve the fluid-structure coupling problem of pore-throat-scale microsphere particles in a fluid grid condition.

Previous studies mainly used sand filling models to evaluate the microsphere plugging performance, and the adaptability of the conclusions obtained in real fractured reservoir cores needs to be verified. At the same time, there are few studies on the plugging mechanism of fractured reservoirs by microspheres using particle flow simulation software. In order to clarify the plugging mechanism of microspheres on fractured oil reservoirs, a specially prepared core model was used to observe the distribution of microspheres in real cores after plugging of microsphere. Then, the microscopic plugging mechanism of microspheres in fractured reservoirs was clarified. Subsequently, particle flow simulation software was used to establish the fluid−solid coupling model of the microsphere plugging, and then, the numerical simulation of the plugging process of microsphere injection was realized by the Python module programming.

Figure 1 shows the idea of the whole study. The specific research content includes the construction of the experimental model and the numerical simulation of microsphere plugging.

2. EXPERIMENTAL EQUIPMENT AND MATERIALS

2.1. Experimental Equipment. A field-emission environmental scanning electron microscope of the FEI Company was used to carry out the microsphere plugging experiments. The device can be used to perform nanoscale stereoscopic observations of the samples without damaging the internal structures of the rock. Meanwhile, the plugging mechanism of the microspheres can be clearly observed.

2.2. Experimental Cores. Figure 2a shows the fractured core slices used in the experiments. The cores used in the experiments were taken from the fractured reservoirs in the ZD area. Standard cylinder samples were selected for the experiments, and the core slices with a thickness of about 2 mm were cut from the core by a cutting machine, and then, the core slices were artificially fractured.

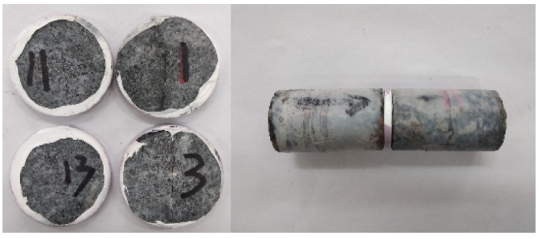

(a) Fractured cores slices (b) Core model

Figure 2. Preparation of the experimental core model.

The current experimental model cannot directly observe the distribution of microspheres inside the real core after the plugging and anti-channeling of microspheres. In order to solve this problem, a special experimental core model was prepared (Figure 2). Two small matrix rock pillars with smooth end faces were selected and artificially fractured, and then, the experimental core slices were placed between the two fractured cores and then placed in the core holder. The end face of the selected cores and core slices are smooth. Only in this way, they can be used to simulate the internal structures of the real cores. The core model was used to conduct the plugging experiments. After the experiments, the core slices were taken out to observe the plugging situation of the microspheres inside the real cores.

2.3. Experimental Scheme. The process of the experiments is as follows: First, excess microsphere solutions were injected into the core model; then, the core slices were taken out and dried, and the plugging situation of the microspheres in the pores was observed with a scanning electron microscope.

https://doi.org/10.1021/acsomega.2c06088
ACS Omega 2022, 7, 46983−46991

3. NUMERICAL SIMULATION MODEL

3.1. Simulation Workflow. First, DEM Software was used to create a rock skeleton particle model representing fractured oil reservoirs, and then, the simulation of the plugging and anti-channeling process by microsphere injection was realized by Python programming. The DEM-DFM algorithm flow used in this model is shown in Figure 3. First, a DEM model is established, and a rock skeleton particle model is generated based on the large particles in the particle aggregates. Then, the porosity and permeability of the rock skeleton grain units are calculated based on the positions of all grains. Assuming that the fluids are incompressible, then the Poisson equation related to the fluid pressure is derived, and the Darcy's law is used to calculate the local flow characteristics. Furthermore, the force of fluids exerted on each microsphere particle during the fluid-structure interaction process was calculated, and the velocity and displacement of the microsphere particles were obtained. The process was repeated, and the fluid grid, permeability, and fluid forces are automatically updated at predetermined intervals. Finally, the calculation stops when the total time step reaches the preset cycle. During the calculation process, the fluid grid is dynamically updated at the predetermined time intervals until the microsphere particles begin to move.

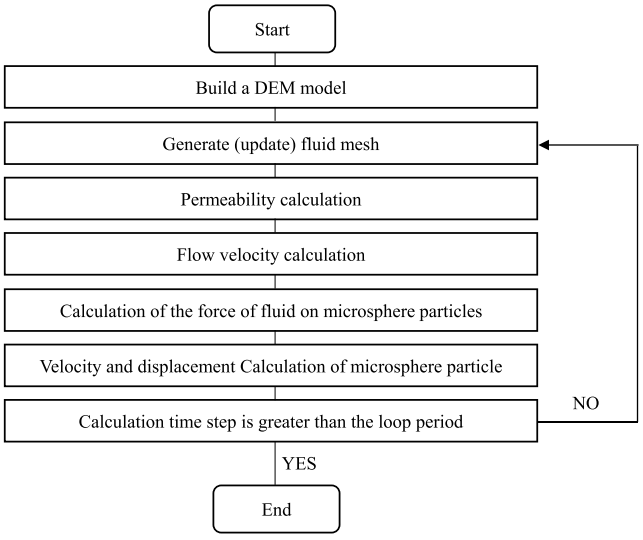

Figure 3. Workflow of DEM-DFM coupling and calculation of microsphere plugging and anti-channeling.

3.2. Establishment of the Fluid−Solid Coupling Model. In the process of numerical simulation, the number of fluid grids needs to be generated first. The number of grids in the xyz directions is 40 × 5 × 10, and the size of each grid in the xyz directions is 500 μm. On the basis of determining the number of fluid grids, the rock skeleton particle model and the plugging and anti-channeling model of microspheres need to be generated as well.

3.2.1. Rock Skeleton Particle Model. Table 1 shows the physical and mechanical properties of rock skeleton particles used to establish the model. The final rock skeleton particle model is shown in Figure 4a. The particle size of the generated rock skeleton particles ranges from 90 to 330 μm. In order to simulate the plugging properties of microspheres in fractured oil reservoirs, T-shaped fractures are generated in the generated rock skeleton particle model by the particle removal method. The final fractured rock skeleton particle model was obtained (Figure 4b).

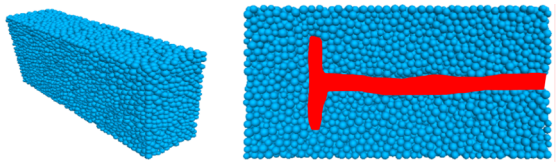

(a) 3D model of rock skeleton particles (b) Fractured rock skeleton particle model

Figure 4. Rock skeleton particle model.

3.2.2. Microsphere Plugging and Anti-channeling Model. Table 2 shows the basic attribute parameters of formation fluids and microsphere particles used to establish the microsphere plugging and anti-channeling model. The final generated microsphere plugging and anti-channeling model is

Table 2. Basic Attribute Parameters of Formation Fluids and Microsphere Particles

parameters	value
size (μm)	60
density (kg/m^3)	1400
stiffness ratio	1.5
fluid viscosity (Pa·s)	1×10^{-3}
fluid density (kg/m^3)	990

Table 1. Physical and Mechanical Properties of Rock Samples

classification	parameter name	parameter value
rock model	size (length × width × height) ($10^3\mu$m)	10 × 2.5×5
	particle size (μm)	90∼330
	fracture width (μm)	300∼500
	porosity	0.3
micromechanical properties of particles	particle density (kg/m^3)	2600
	particle normal stiffness (GPa)	1
	particle contact stiffness ratio	1.5
	particle tangential stiffness	normal stiffness /1.5
	sliding friction coefficient between particles	0.5
	bond tensile strength (MPa)	50
	bond stiffness ratio	1.8
	bond friction angle	45°

https://doi.org/10.1021/acsomega.2c06088
ACS Omega 2022, 7, 46983−46991

shown in Figure 5. It shows the situation when the microspheres have not entered the rock skeleton particles.

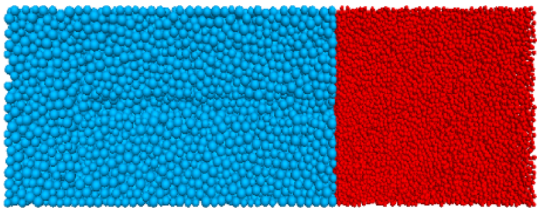

Figure 5. Plugging and anti-channeling model of microspheres.

Under the action of hydrodynamic force, the microsphere particles begin to enter into the rock skeleton particles. Because the rock skeleton particles themselves are very dense, the microsphere particles mainly enter the core along the T-shaped fractures. After the microsphere particles enter the formation and come into contact with the rock skeleton particles, the migration speed and direction of the microsphere particles will change, and the force of the microsphere particles in the fluids will also change, and this change will change with the cycle of the calculation time step, and then, the data will be updated automatically. By changing the injection pressure difference, fracture width, and particle size ratio, the effects of different factors on the process of microsphere plugging and anti-channeling were obtained.

4. EXPERIMENTAL AND SIMULATION RESULTS

4.1. Experimental Results. The microspheres enter the pores with the solution in the form of suspended particles. The microspheres preferentially enter the areas with developed fractures and high permeability and then migrate into the pores. Since the microsphere particles are affected by surface adsorption, mechanical trapping, hydrodynamic trapping, and the interaction between the elastic microsphere particles during the migration process,[27,28] a retention phenomenon will occur in the microsphere system on the surface of pores and inside the throats. In this experiment, the plugging state of the microspheres after entering the core was directly observed using a scanning electron microscope (Figures 6−10).

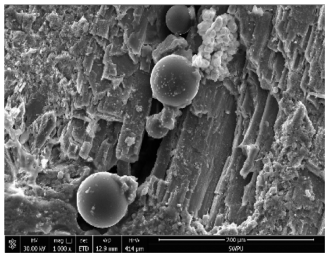

Figure 6. Direct microsphere plugging.

According to the results shown in the Figures 6−10, the microscopic plugging mechanism of microspheres in fractured reservoir cores was clarified, including direct microsphere plugging, cluster bridging plugging, adhesion plugging, extrusion-deformation plugging, and extrusion-crushing plugging.

4.1.1. Direct Plugging by Single Microspheres. Figure 6 shows the case where a single microsphere directly plugs the fractures. When the pore throat size is smaller than the particle size of a single microsphere particle, the microsphere particles

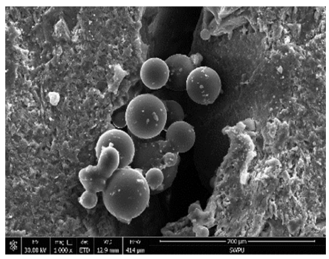

Figure 7. Bridging plugging of microsphere clusters.

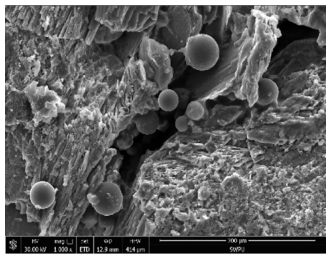

Figure 8. Microspheres are adhered to the matrix and surface of the pores.

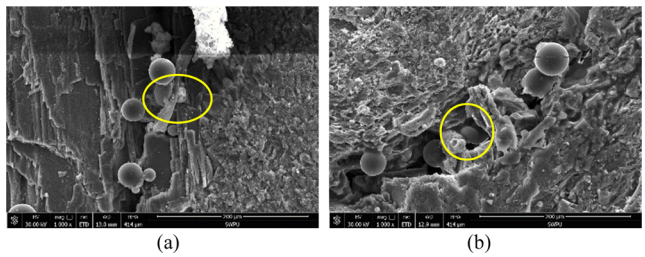

(a) (b)

Figure 9. (a) Extrusion-deformation and plugging of microspheres and (b) microspheres returning to a spherical shape.

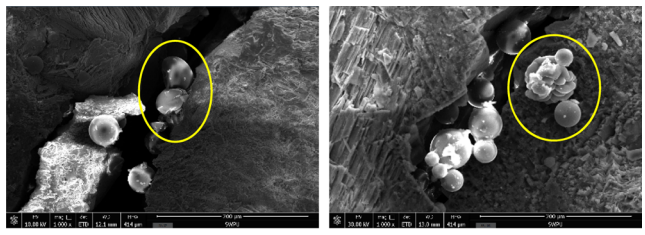

(a) (b)

Figure 10. (a) Extrusion-crushing plugging of microspheres and (b) crushed microspheres reform into smaller microspheres.

are trapped by the pore throat and then will stay at the entrance of the pore throat to form a blockage. Pore throat size, microsphere particle size, microsphere concentration, and fluid flow rate all will affect the plugging of a single microsphere. When the pore throat size remains unchanged, the larger the microsphere particle size, the smaller the concentration of the microspheres, the greater the fluid flow rate, and the plugging of single microspheres is more likely to occur.[29,30]

4.1.2. Bridging Plugging of Microsphere Clusters. Figure 7 shows the situation of the microsphere clusters bridging plugging in the fractures. When the pore throat size is larger than the particle size of the microspheres, multiple microsphere particles aggregate together through secondary cross-linking to form microsphere clusters and then the plugging will

https://doi.org/10.1021/acsomega.2c06088
ACS Omega 2022, 7, 46983−46991

form. Pore throat size, particle size of microspheres, number of microspheres, elastic deformation capacity of microspheres, and cross-linking strength of microspheres all affect the strength of bridging plugging of microspheres. When other conditions remain unchanged, the greater the number of microspheres, the higher the cross-linking strength between the microsphere particles, and the greater the strength of the bridging plugging of microsphere cluster.

4.1.3. Adhesion Plugging. Figure 8 shows the case in which the microspheres adhered to the matrix and fracture surfaces. It is actually because the microsphere particles are in a state of mechanical equilibrium, and the resultant force of the microspheres points to the rock surface so that the microspheres adhere to the matrix or fracture surface. The adhesion of microspheres will reduce the cross-sectional area of the channel and increase the roughness of the surface of the channel, thereby increasing the seepage resistance and conductive to plugging. Only when this force balance is broken, such as when the fluid velocity changes, the adhesion state of the microspheres will change.

4.1.4. Extrusion-Deformation and Extrusion-Crushing of Microsphere Plugging. Figure 9 shows the situation of plugging after the microspheres are squeezed and deformed. The microsphere particles will be subject to the driving force of the fluids and the reaction force acting on the throat wall. When the driving force of the microspheres is greater than the reaction force of the throat wall, because the microsphere particles have a certain elasticity, the microsphere particles will elastically deform and squeeze into the pore throats, resulting in seepage resistance. The spherical shape is restored only when the microsphere particles pass through the pore throats. As shown in Figure 9a, the microspheres in the circle are undergoing extrusion deformation, and Figure 9b shows that the microspheres return to a spherical shape after passing through the pore throats. The factors affecting the extrusion deformation of the microspheres are the force among microspheres, the size of pore throats and microspheres, and the elasticity of the microspheres. When other conditions remain unchanged, the greater the driving force, the easier the microspheres pass through the core pore throats.

Figure 10 shows the situation of plugging after the microspheres are squeezed and crushed. When the microsphere particles pass through the pore throats, if the driving force of the microsphere particles is too large and the pore throat size is small enough, the microspheres will be crushed because there is no time to have elastic deformation, as shown in Figure 10a; the crushed microspheres will reform into smaller microspheres after passing through the pore throats, as shown in Figure 10b.

4.2. Numerical Simulation Results. In this simulation process, $1-2 \times 10^6$ time steps are calculated, and each time step is 2×10^{-8} s. In this study, the effects of injection pressure difference, fracture width, and particle size ratio on the plugging effect were compared.

4.2.1. Effect of Particle Size Ratio on Plugging. In order to study the effect of particle size ratio on the plugging and anti-channeling of microspheres while keeping other factors the same (with an injection pressure difference of 1.5 MPa and a fracture width of 450 μm), the particle size ratios of rock skeleton particles and microspheres were calculated, respectively, when the particle size ratios were 1.5−2.5, 2.5−3.5, 3.5−4.5, and 4.5−5.5. Figure 11 shows the final numerical simulation calculation results of plugging and anti-channeling

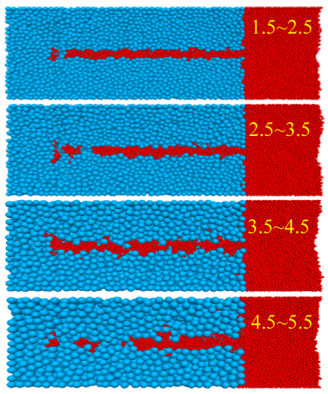

Figure 11. Effect of particle size ratio on plugging and anti-channeling of microspheres.

of microspheres under different particle size ratios. It can be seen that the larger the particle size ratio, the more dispersed the microspheres when they enter the fractures and pores and the worse the plugging effect will be. This is because as the particle size ratio increases, the pores between the rock skeleton particles also become larger, resulting in the subsequent injection of microspheres directly going into the cores through these pores.

4.2.2. Influence of Injection Pressure Difference on Plugging. In order to study the effect of injection pressure difference on the plugging and anti-channeling of microspheres, under the same conditions (with a fracture width of 500 μm and a particle size ratio of 2.5−3.5), the simulation was conducted under injection pressure differences of 0.5, 0.75, 1.0, 1.25, 1.5 MPa. Figure 12 shows the final numerical simulation

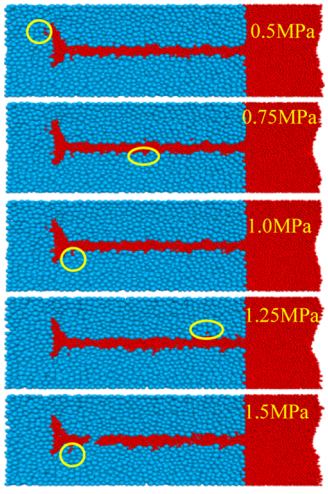

Figure 12. Influence of injection pressure difference on plugging and anti-channeling of microspheres.

calculation results of microsphere plugging and anti-channeling under different injection pressure differences. It can be seen that the final plugging forms of microspheres entering core fractures under different injection pressure differences are similar. In Figure 12, there are microsphere particles in the yellow circles around the core fractures, which indicates that when the fracture width is 500 μm and the particle size ratio is between 2.5 and 3.5, a small amount of microsphere particles can enter the pores between the rock skeleton particles by extrusion deformation or crushing, and it can be observed that

https://doi.org/10.1021/acsomega.2c06088
ACS Omega 2022, 7, 46983−46991

the microsphere particles entering between the rock skeleton particles can directly realize plugging with single microsphere particles, and there are also multiple microsphere particles that form cluster bridging plugging.

4.2.3. Influence of Fracture Width on Plugging. In order to study the effect of fracture width on plugging and anti-channeling of microspheres, the simulation process was conducted under the same condition of a pressure of 1.5 MPa and a particle size ratio of 2.5−3.5 and under fracture widths of 300, 350, 400, 450, and 500 μm. Figure 13 shows the final numerical simulation calculation results of microsphere plugging and anti-channeling under different fracture widths. It can be seen that the plugging forms of microspheres entering the core fractures under different fracture widths are quite different. When the fracture width is 300 μm, there are very few microsphere particles entering the core fracture pores, which indicates that for this simulation process, the fracture width should be set above 300 μm, otherwise the real microsphere plugging and anti-channeling process cannot be simulated. With the increase in fracture width, more and more microspheres enter the fracture and participate in the sealing process.

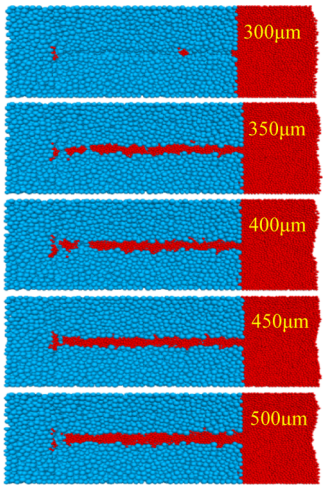

Figure 13. Influence of fracture width on plugging and anti-channeling of microspheres.

5. DISCUSSION

5.1. Influence of Particle Size Ratio on the Plugging and Anti-channeling Mechanism of Microspheres. In this study, direct microsphere plugging, cluster bridging plugging, adhesion plugging, extrusion-deformation plugging, and extrusion-crushing plugging were observed under the microscope. Through the numerical simulation study, we found that the particle plugging process is similar to the experimental results. The experimental results given in Figure 14a−d are in good agreement with the numerical simulation results.

Figure 15 shows a cross-sectional view of pores among rock skeleton grains. The diameter of the inscribed circle in the cross section of the rock skeleton particle is calculated according to the following formula[31−33]

$$D = \frac{2}{3}\left(L_1 + L_2 + L_3 - \frac{1}{2}(D_1 + D_2 + D_3)\right) \quad (1)$$

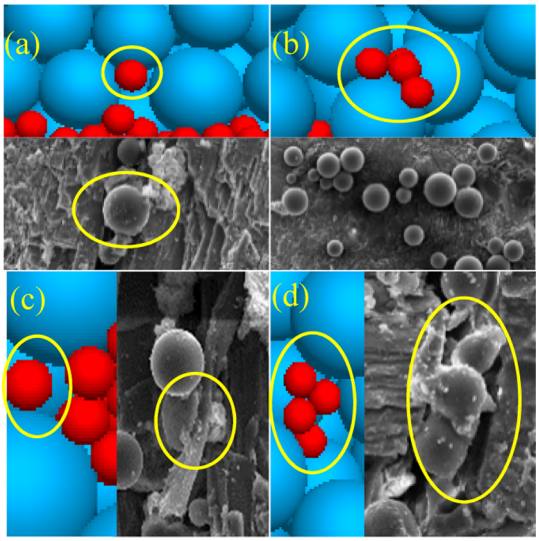

Figure 14. (a) Direct microsphere plugging, (b) adhesion plugging, (c) extrusion-deformation plugging, and (d) cluster bridging plugging.

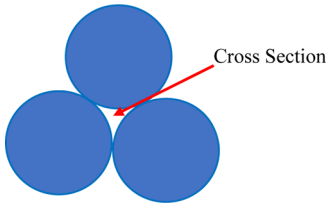

Figure 15. Schematic diagram of the cross section of pores among rock skeleton particles.

Where D represents the diameter of the inscribed circle (μm); L_1, L_2, and L_3 represent the distance between the center of the inscribed circle and the centroid of the rock skeleton particle (μm); and D_1, D_2, and D_3 represent the diameter (μm) of the three rock skeleton particles forming the inscribed circle.

If the diameters of the three rock skeleton particles forming the inscribed circle are equal, then $L_1 = L_2 = L_3$ and $D_1 = D_2 = D_3$, and by substituting this into eq 1, we can obtain

$$D = 0.1547D_0 \quad (2)$$

where D_0 represents the particle diameter of the rock skeleton (μm).

Also, when the diameter of the three rock skeleton particles forming the inscribed circle is the smallest, the smallest diameter of the inscribed circle can be obtained; when the diameter of the three rock skeleton particles forming the inscribed circle is the largest, the largest diameter of the inscribed circle can be obtained. In this simulation process, due to the limitation of the calculation ability of software, combined with the actual simulation situation, the particle size of the microspheres is set to 60 μm, and then, the particle diameter of the rock skeleton is obtained according to the set particle size ratio. The range is 90−330 μm, compared to the real core, and this is equivalent to enlarging the microspheres and rock pores at the same time, so the conclusions obtained from this calculation are consistent with the previous experiments. According to eq 2, the diameter of the inscribed circle between the rock skeleton particles can range from 13.92 to 51.05 μm, and the diameter of the pore throat formed between the rock skeleton particles is between 13.92 and 51.05

https://doi.org/10.1021/acsomega.2c06088
ACS Omega 2022, 7, 46983−46991

μm. The ratio of microsphere particle size to core pore throat diameter α was obtained (Table 3).

Table 3. Distribution Range of the Diameter of the Inscribed Circle

particle size ratio	range of rock skeleton particle diameter (μm)	range of pore throat diameter (μm)	ratio of microsphere particle size to core pore throat diameter (α)
1.5−2.5	90−150	13.92−23.21	2.59−4.31
2.5−3.5	150−210	23.21−32.49	1.85−2.59
3.5−4.5	210−270	32.49−41.77	1.44−1.85
4.5−5.5	270−330	41.77−51.05	1.18−1.44

Combining with Figure 14, the pores of the rock skeleton can be further regarded as the extension of fractures, that is, tiny fractures or dominant channels with narrow width. When the particle size ratio is 1.5−2.5, that is, when the ratio of microsphere particle size to fracture or dominant channel radius meets $2.59 < \alpha < 4.31$, almost no microsphere particles enter between the rock skeleton particles except for fractures, indicating that the microspheres directly plug the fractures; when the particle size ratio meets 2.5−4.5, that is, $1.44 < \alpha < 2.59$, a small amount of microsphere particles enter the microfractures between the rock skeleton particles except for the large fractures, and the larger the particle size ratio is, the more microsphere particles enter the microfractures, indicating that the microspheres can pass through fractures by extrusion deformation (and maybe crushing) and then plug the smaller pores; when the particle size ratio meets 4.5−5.5, that is, $1.18 < \alpha < 1.44$, a large number of microsphere particles enter the tiny fractures between the rock skeleton particles except for the fractures, but the microspheres have no substantial sealing effect at this time; and when $\alpha < 1.18$ or even smaller, the plugging of microspheres is ineffective.

5.2. Factors Influencing the Filling Rates. Here, the change in the microsphere filling rate ω is used to characterize the filling degree of the microsphere particles in the fracture pores. It reflects the reduction degree of the fracture porosity, that is, the increase in the filling rate indicates the decrease in the porosity. The higher the filling rate is, the better the plugging effect is, and the fill rate is calculated as follows

$$\omega = \frac{\sum_{i=1}^{N} V_i}{\sum_{j=1}^{N} V_j} \tag{3}$$

where V_i represents the volume of microsphere particles (μm^3) and V_j represents the fracture pore volume (μm^3).

5.2.1. Particle Size Ratio. It can be found from Figure 16 that in some cases, the percentage of microsphere particles filled has a certain abrupt increase, especially in the early stage of the stable interval. The formation of step-by-step plugging and anti-channeling in the middle period make the injection pressure fluctuate, so that the filling curve will also fluctuate. As more and more microsphere particles enter the pores, this fluctuation becomes less and less obvious and eventually tends to be stable. This phenomenon also exists in the practical applications. However, with the progress of numerical simulation calculation, this phenomenon gradually decreases. At the same time, it can be found that the larger the particle size ratio, the more obvious the fluctuation will be. This is because the number of microspheres entering between the rock skeleton particles increases, while that entering the fractures decreases, resulting in a decrease in the final filling rate of microspheres in the fractures.

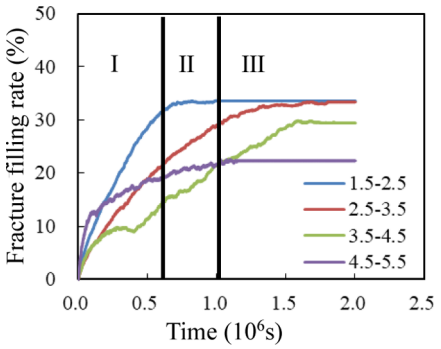

Figure 16. Effect of particle size ratio on fracture filling rate (I, initial stage; II, fluctuation stage; and III, stable stage).

It can be seen from Figure 16 that the model with a larger particle size ratio has a smaller final fracture filling rate, while the model with a larger particle size ratio has a longer deceleration stage and more obvious fluctuations. It can be seen from the two curves in Figure 15 that the fluctuation phenomenon started very early and continued to appear in the middle stage, so the final curve was jagged. The fracture filling rate reflects the degree of reduction of the fracture porosity. In Figure 17, it can be seen that the particle size ratio is negatively correlated with the filling rate of microspheres in the fracture, and the final fracture filling rate in the fracture decreases linearly with the particle size ratio, that is, the larger the particle size ratio is, the smaller the decrease in the porosity of core fractures is and the worse the plugging effect will be.

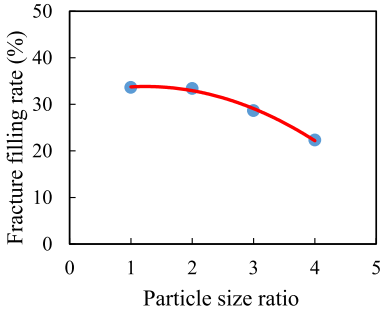

Figure 17. Relationship between particle size ratio and fracture filling rate.

5.2.2. Injection Pressure Difference. It can be seen from Figure 18 that in the initial stage of microsphere injection, with the increase in injection pressure difference, the faster the filling rate of fractures grows, the shorter the deceleration stage of the curve becomes, and the time for the final stabilization becomes shorter. Figure 19 shows that the pressure gradient is positively correlated with the filling rate of microspheres in the fracture, and the final fracture filling rate increases linearly with the injection pressure difference, that is, the greater the injection pressure difference is, the greater the final fracture filling rate is, the greater the decrease in fracture porosity is, and the better the plugging effect will be. Therefore, an injection pressure difference of 1.5 MPa is taken as the standard value for the simulation.

5.2.3. Fracture Width. It can be seen from Figure 20 that in the initial stage of microsphere injection, as the fracture width

https://doi.org/10.1021/acsomega.2c06088
ACS Omega 2022, 7, 46983−46991

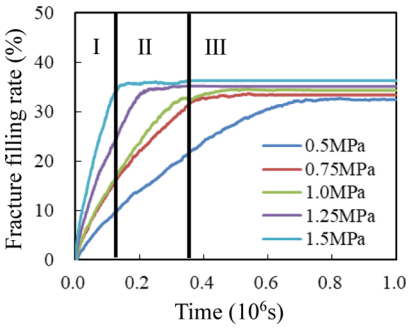

Figure 18. Effect of injection pressure difference on fracture filling rate (I, initial stage; II, fluctuation stage; and III, stable stage).

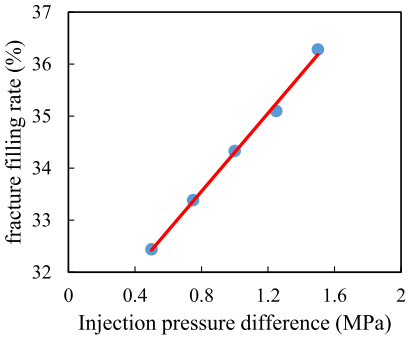

Figure 19. Relationship between injection pressure difference and fracture filling rate.

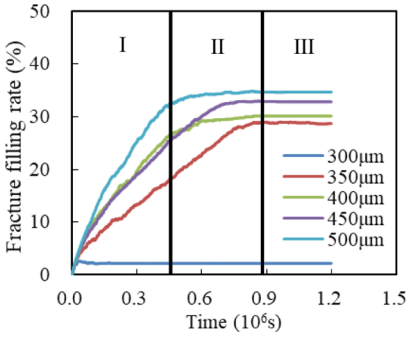

Figure 20. Effect of fracture width on fracture filling rate (I, initial stage; II, fluctuation stage; and III, stable stage).

increases, the increase in fracture filling rate becomes faster, the deceleration stage of the curve becomes shorter, and the final stabilization time becomes shorter as well. The fracture filling rate reflects the degree of reduction of fracture porosity. In Figure 21, it can be seen that the fracture width is positively correlated with the filling rate of microspheres in the fracture. The final fracture filling rate increases linearly with the fracture width, that is, the larger the fracture width is, the greater the final fracture filling rate is, and the decrease in core fracture porosity is greater, and the plugging effect is better.

6. SUMMARY AND CONCLUSIONS

Through this study, the following conclusions are drawn:

(1) The microscopic plugging mechanism of microspheres in fractured reservoirs was clarified, including direct microsphere plugging, cluster bridging plugging, adhesion plugging, extrusion-deformation plugging, and extrusion-crushing plugging.

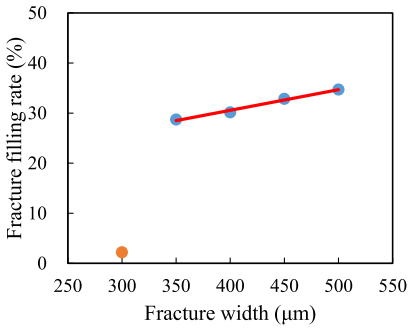

Figure 21. Relationship between fracture width and fracture filling rate.

(2) Based on particle flow simulation software, the fluid−solid coupling model of plugging and anti-channeling of microspheres was established, and then, the simulation of the process of plugging and anti-channeling by microsphere injection was realized by the Python programming.

(3) When the ratio of the microsphere particle size to fracture is $2.59 < \alpha < 4.31$, the pores are directly plugged; when $1.44 < \alpha < 2.59$, the microspheres can pass through the fractures through extrusion-deformation and extrusion-crushing, and then, the smaller pores are plugged; when $1.18 < \alpha < 1.44$, the microspheres have no substantial plugging effect; and when $\alpha < 1.18$, plugging will not occur.

(4) The numerical simulation results of plugging and anti-channeling by microsphere injections show that the smaller the particle size ratio, the greater the injection pressure difference, the fracture width, and the reduction magnitudes in fracture porosity and core permeability and the higher the plugging rate.

(5) Due to the functional limitations of the current numerical simulation software, it cannot simulate the heterogeneous situation. Therefore, there is still a certain deviation between the numerical simulation results based on the equivalent method and the actual plugging situation of microspheres. In the future, we will try to develop new algorithm schemes to seek the optimal equivalent simulation method considering the homogeneity.

AUTHOR INFORMATION

Corresponding Author

Renyi Lin − *Geological Resources and Geological Engineering Post-doctoral Research Station, Chengdu University of Technology, Chengdu 610059 Sichuan, China; College of Energy, Chengdu University of Technology, Chengdu 610059 Sichuan, China;* orcid.org/0000-0003-4058-1383; Email: 543663589@qq.com

Author

Lei Sun − *State Key Laboratory of Oil and Gas Reservoir Geology and Exploitation, Southwest Petroleum University, Chengdu 610500 Sichuan, China*

Complete contact information is available at: https://pubs.acs.org/10.1021/acsomega.2c06088

Notes

The authors declare no competing financial interest.

https://doi.org/10.1021/acsomega.2c06088
ACS Omega 2022, 7, 46983−46991

■ ACKNOWLEDGMENTS

This research was supported by the 13th Five-Year National Major Special Project of China (no. 2016ZX05048-004-005).

■ REFERENCES

(1) Tian, Y.; Uzun, O.; Shen, Y. Feasibility study of gas injection in low permeability reservoirs of Changqing oilfield. *Fuel* **2020**, *274*, 117831.
(2) Davarpanah, A.; Mirshekari, B.; Razmjoo, A. A. A simulation study of water injection and gas injectivity scenarios in a fractured carbonate reservoir: A comparative study. *Pet. Res.* **2019**, *4*, 250−256.
(3) Yang, H.; Kang, W.; Yin, X.; Tang, X.; Song, S.; Lashari, Z. A.; Bai, B.; Sarsenbekuly, B. Research on matching mechanism between polymer microspheres with different storage modulus and pore throats in the reservoir. *Powder Technol.* **2017**, *313*, 191−200.
(4) Sun, H.; Wang, T.; Xiao, J. Novel polymer microspheres step-by-step deep profile control technology. *Oil Gas Geol. Recovery* **2006**, *13*, 77−79.
(5) Lei, G.; Zheng, J. Synthesis of pore-throat-scale polymer microspheres and research on new technology of full profile control and flooding. *J. China Univ. Pet.* **2007**, *31*, 87−90.
(6) Pingya, L.; Lei, S.; Sun, L. Blocking characteristics of microgel in high-temperature and high-salinity water producing gas reservoirs: An experimental study. *Nat. Gas. Ind.* **2018**, *38*, 69−75.
(7) Liu, C.; An, Y. Research on deep profile control technology of polymer microspheres and mine practice. *Drill. Prod. Technol.* **2010**, *33*, 62−64.
(8) Fan, Z.; Cheng, L. Visualization and field test of seepage field for profile control plugging with polymer microspheres. *Sci. Technol. Eng.* **2012**, *12*, 7543−7546.
(9) Shi, J.; Varavei, A.; Huh, C.; Delshad, M.; Sepehrnoori, K.; Li, X. Transport model implementation and simulation of microgel processes for conformance and mobility control purposes. *Energy Fuels* **2011**, *25*, 5063−5075.
(10) Shi, J.; Varavei, A.; Huh, C.; Delshad, M.; Sepehrnoori, K.; Li, X. Viscosity model of preformed microgels for conformance and mobility control. *Energy Fuels* **2011**, *25*, 5033−5037.
(11) Kloss, C.; Goniva, C.; Hager, A.; Amberger, S.; Pirker, S. Models, algorithms and validation for opensource DEM and CFD-DEM. *Prog. Comput. Fluid Dynam. Int. J.* **2012**, *12*, 140−152.
(12) Tabib, M. V.; Roy, S. A.; Joshi, J. B. CFD simulation of bubble column-An analysis of interphase forces and turbulence models. *Chem. Eng. J.* **2008**, *139*, 589−614.
(13) Tao, H.; Tao, J. Quantitative analysis of piping erosion micro-mechanisms with coupled CFD and DEM method. *Acta Geotech.* **2017**, *12*, 573−592.
(14) Guo, Y.; Yu, X. Comparison of the implementation of three common types of coupled CFD-DEM model for simulating soil surface erosion. *Int. J. Multiphase Flow* **2017**, *91*, 89−100.
(15) Climent, N.; Arroyo, M.; O'Sullivan, C.; Gens, A. Sand production simulation coupling DEM with CFD. *Eur. J. Environ. Civ. Eng.* **2014**, *18*, 983−1008.
(16) Hu, Z.; Zhang, Y.; Yang, Z. Suffusion-induced deformation and microstructural change of granular soils: a coupled CFD-DEM study. *Acta Geotech.* **2019**, *14*, 795−814.
(17) Ding, W. T.; Xu, W. J. Study on the multiphase fluid-solid interaction in granular materials based on an LBM-DEM coupled method. *Powder Technol.* **2018**, *335*, 301−314.
(18) Kruggel-Emden, H.; Kravets, B.; Suryanarayana, M. K.; Jasevicius, R. Direct numerical simulation of coupled fluid flow and heat transfer for single particles and particle packings by a LBM-approach. *Powder Technol.* **2016**, *294*, 236−251.
(19) Cui, X.; Li, J.; Chan, A.; Chapman, D. Coupled DEM-LBM simulation of internal fluidisation induced by a leaking pipe. *Powder Technol.* **2014**, *254*, 299−306.
(20) Brumby, P. E.; Sato, T.; Nagao, J.; Tenma, N.; Narita, H. Coupled LBM-DEM Micro-scale Simulations of Cohesive Particle Erosion Due to Shear Flows. *Transport Porous Media* **2015**, *109*, 43−60.
(21) Zhang, F.; Wang, T.; Liu, F. Modeling of fluid-particle interaction by coupling the discrete element method with a dynamic fluid mesh: Implications to suffusion in gap-graded soils. *Comput. Geotech.* **2020**, *124*, 103617.
(22) Mcdowell, G. R.; De Bono, B.; Yue, P.; Yu, H.-S. Micro mechanics of isotropic normal compression. *Géotech. Lett.* **2013**, *3*, 166−172.
(23) Holmes, D. W.; Williams, J. R.; Tilke, P. Smooth particle hydrodynamics simulations of low Reynolds number flows through porous media. *Int. J. Numer. Anal. Methods GeoMech.* **2011**, *35*, 419−437.
(24) Zhang, F.; Dontsov, E.; Mack, M. Fully coupled simulation of a hydraulic fracture interacting with natural fractures with a hybrid discrete-continuum method. *Int. J. Numer. Anal. Methods GeoMech.* **2017**, *41*, 1430−1452.
(25) Zhang, F.; Damjanac, B.; Maxwell, S. Investigating hydraulic fracturing complexity in naturally fractured rock masses using fully coupled multiscale numerical modeling. *Rock Mech. Rock Eng.* **2019**, *52*, 5137−5160.
(26) Itasca Consulting Group Inc. PFC3D (Particle flow code in 3 dimensions), Version 5.0, Documentation set of version 6.00.55: Minneapolis Itasca, 2015; pp 1−10.
(27) Yao, C.*Experimental and simulation study on the seepage mechanism of elastic microspheres at the pore-throat scale*; China University of Petroleum, 2014; pp 1−5.
(28) Bradford, S. A.; Torkzaban, S. Colloid Transport and Retention in Unsaturated Porous Media: A Review of Interface-, Collector-, and Pore-Scale Processes and Models. *Vadose Zone J.* **2008**, *7*, 667−681.
(29) Chauveteau, G.; Nabzar, L.; Coste, J.-P. Physics and modeling of permeability damage induced by particle deposition. *SPE J.* **1998**, 409−419.
(30) Veerapen, J. P.; Nicot, B.; Chauveteau, G. A. In-depth permeability damage by particle deposition at high flow rates. *SPE J.* **2001**, 516−527.
(31) Ergun, S. Fluid flow through packed columns. *Chem. Eng. Prog.* **1952**, *48*, 89−94.
(32) Liu, Y. F.; Tang, Y. F.; Chang, Q. H.; Ma, C. T.; He, S. H.; Yuan, L. Development of a novel heat- and shear-resistant nano-silica gelling agent. *Nanotechnol. Rev.* **2022**, *11*, 2786−2799.
(33) Olayiwola, S. O.; Dejam, M. Synergistic interaction of nanoparticles with low salinity water and surfactant during alternating injection into sandstone reservoirs to improve oil recovery and reduce formation damage. *J. Mol. Liq.* **2020**, *317*, 114228.

https://doi.org/10.1021/acsomega.2c06088
ACS Omega 2022, 7, 46983−46991